GEOPHYSICS, VOL. 70, NO. 3 (MAY-JUNE 2005); P. U19–U27, 14 FIGS.
10.1190/1.1925749

Wave-equation migration velocity analysis by focusing diffractions and reflections

Paul C. Sava[1], Biondo Biondi[2], and John Etgen[3]

ABSTRACT

We propose a method for estimating interval velocity using the kinematic information in defocused diffractions and reflections. We extract velocity information from defocused migrated events by analyzing their residual focusing in physical space (depth and midpoint) using prestack residual migration. The results of this residual-focusing analysis are fed to a linearized inversion procedure that produces interval velocity updates. Our inversion procedure uses a wavefield-continuation operator linking perturbations of interval velocities to perturbations of migrated images, based on the principles of wave-equation migration velocity analysis introduced in recent years. We measure the accuracy of the migration velocity using a diffraction-focusing criterion instead of the criterion of flatness of migrated common-image gathers that is commonly used in migration velocity analysis. This new criterion enables us to extract velocity information from events that would be challenging to use with conventional velocity analysis methods; thus, our method is a powerful complement to those conventional techniques.

We demonstrate the effectiveness of the proposed methodology using two examples. In the first example, we estimate interval velocity above a rugose salt top interface by using only the information contained in defocused diffracted and reflected events present in zero-offset data. By comparing the results of full prestack depth migration before and after the velocity updating, we confirm that our analysis of the diffracted events improves the velocity model. In the second example, we estimate the migration velocity function for a 2D, zero-offset, ground-penetrating radar data set. Depth migration after the velocity estimation improves the continuity of reflectors while focusing the diffracted energy.

INTRODUCTION

Seismic reflection wavefields consist of specular reflections from laterally smooth and continuous surfaces and nonspecular diffractions from sharp lateral changes of reflectivity. Reflecting surfaces can also be subclassified as surfaces with small radii of curvature and surfaces with large radii of curvature. Zero-offset specular reflections from surfaces with large radii of curvature contain no usable velocity information. In contrast, diffractions and specular reflections from surfaces with small radii of curvature contain substantial information about the accuracy of the velocity model. Essentially, when the migration velocity function is correct, diffractions collapse to points, and curved surfaces have minimal defocusing.

Surfaces with small radii of curvature introduce discontinuities that generate diffractions. Thus, achieving minimal defocusing and collapsing all diffractions can be seen as complementary sides of the same problem. Conceptually, a reflector is a linear superposition of neighboring diffractors. When data corresponding to such a reflector composed of point scatterers are migrated with the correct velocity, all diffractions focus to points. If the migration velocity is incorrect, diffractions do not collapse, and defocused events result.

Figures 1–3 illustrate the situations described in the preceding paragraphs. The three panels in each figure correspond to migration of seismic data with different velocities: (a) migration with high velocity, (b) migration with correct velocity, and (c) migration with low velocity. The smooth reflector in Figure 1 is changing the position function of velocity, but we have no indication of which velocity is correct. In contrast, the images of reflectors in Figures 2 and 3 clearly indicate velocity inaccuracy. The defocused syncline in Figure 2 as well as

Manuscript received by the Editor March 25, 2004; revised manuscript received September 20, 2004; published online May 23, 2005.
[1]Formerly with Stanford University, Stanford Exploration Project, Geophysics Department, Stanford, California 94305-2215; presently with the University of Texas–Austin, Bureau of Economic Geology, University Station, Box X, Austin, Texas 78713-8924. E-mail: paul.sava@beg.utexas.edu.
[2]Stanford University, Stanford Exploration Project, Geophysics Department, Stanford, California 94305-2215. E-mail: paul@sep.stanford.edu; biondo@sep.stanford.edu.
[3]BP, E&P Technology Group, 200 Westlake Park Boulevard, Houston, Texas 77079-2696. E-mail: john.etgen@bp.com.

the uncollapsed diffractions at reflector truncations shown in Figure 3 indicate velocity inaccuracies.

Focusing information is often present in seismic and ground-penetrating radar (GPR) wavefields, but it is not commonly used for velocity analysis. The conventional alternative relies on moveout information obtained by analysis of multioffset data. However, the information carried by defocused energy is different and complementary to the information obtained from moveout analysis, and it should be used to further constrain the velocity models. The goal of this article is to present such a methodology for estimating interval velocities from information contained in defocused reflections and diffractions.

Migration velocity analysis (MVA) using diffracted events is not a new concept. Harlan et al. (1984) address this problem and propose methods to isolate diffraction events around faults, quantify focusing by the use of statistical tools, and introduce velocity analysis techniques applicable to simple geology, e.g., constant velocity or $v(z)$. Similarly, de Vries and Berkhout (1984) use the concept of minimum entropy to evaluate diffraction focusing. They apply this methodology to velocity analysis, again for the case of simple geology. Soellner and Yang (2002) focus diffractions simulated by using data-derived parameters to estimate interval velocities.

Sava and Biondi (2004a,b) introduce a method of MVA using wave-equation techniques to improve the quality of migrated images, mainly by correcting moveout inaccuracy of specular reflections. Wave-equation MVA finds a slowness perturbation that corresponds to an image perturbation. This method is similar to ray-based migration tomography (Al-Yahya, 1989; Stork, 1992; Etgen, 1993) where the slowness perturbation is derived from depth errors, and to wave-equation inversion (Tarantola, 1986) or wave-equation tomography (Woodward, 1992; Pratt, 1999; Dahlen et al., 2000) where the slowness perturbation is derived from measured wavefield perturbations.

The moveout information given by the specular reflections is not the only information contained by an image migrated with the incorrect velocity. Nonspecular diffracted energy and specular reflections from curved interfaces are present in the migrated images and clearly indicate velocity inaccuracies. Traveltime-based MVA methods do not easily deal with the diffraction energy and are mostly concerned with moveout analysis. An exception is stereotomography (Billette et al., 2003), which accounts for both reflected and diffracted events. In contrast, a difference between an inaccurate image and a perfectly focused target image contains both specular and nonspecular energy; therefore, wave-equation MVA is naturally able to derive velocity updates based on both of these types of information. Our proposed method can benefit, and thus be used in conjunction with, methods to isolate diffracted energy from seismic data (Papziner and Nick, 1998; Landa and Keydar, 1998; Khaidukov et al., 2004).

In this article, we use wave-equation MVA (Biondi and Sava, 1999; Sava and Fomel, 2002; Sava and Biondi, 2004a,b) to estimate slowness updates based on focusing analysis using residual migration. With residual migration, we create from a reference image a family of images corresponding to various

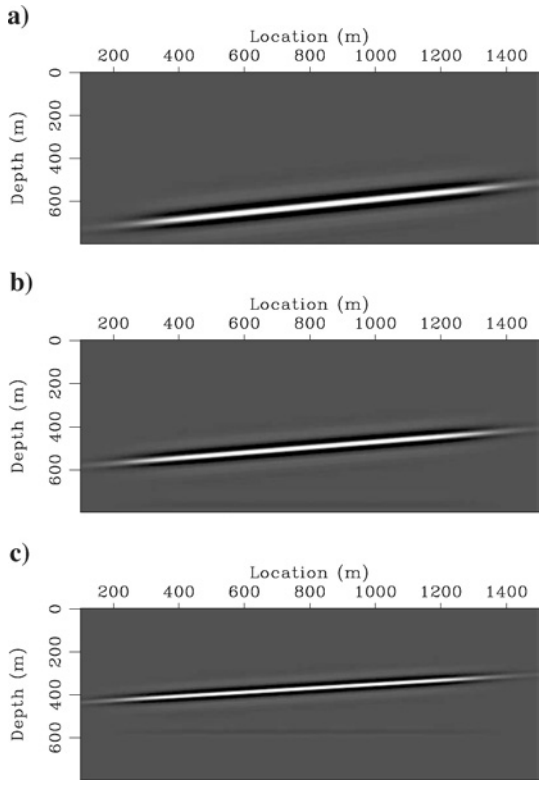

Figure 1. Migration of data generated from an earth model without sharp truncations and high reflector curvature. Images obtained by wave-equation migration with (a) fast velocity, (b) correct velocity, and (c) slow velocity.

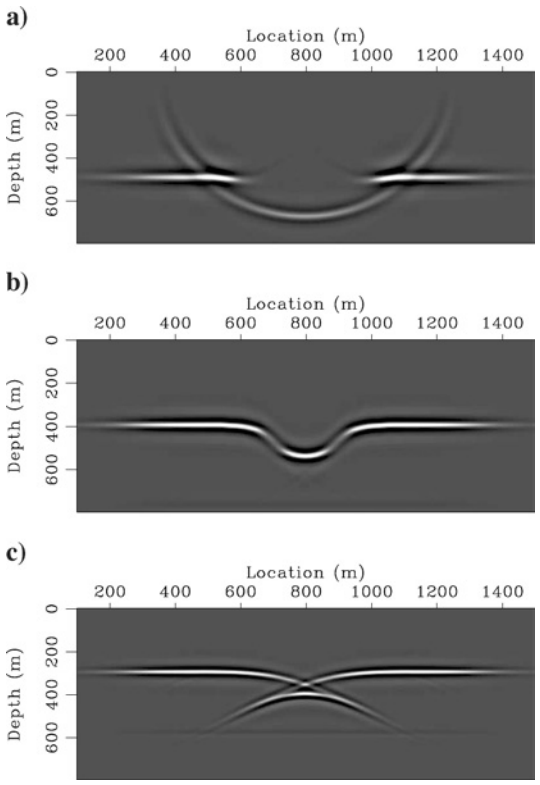

Figure 2. Migration of data generated from an earth model with high reflector curvature. Images obtained by wave-equation migration with (a) fast velocity, (b) correct velocity, and (c) slow velocity.

velocities of known ratios to a reference velocity. The best focused image is interpreted by picking the optimal value of this ratio, or residual focusing parameter, at every spatial location.

One application of this technique in seismic imaging concerns areas with abundant, clearly identifiable diffractions and reflectors with small radii of curvature. Examples include highly fractured reservoirs, carbonate reservoirs, rough salt bodies, and reservoirs with complicated stratigraphic features. Another application is related to imaging of constant-offset GPR data, where moveout analysis is not an option. For multioffset GPR data, we can use conventional moveout-based processing (Vasco et al., 1997; Pipan et al., 2003).

Of particular interest for this methodology is the case of salt bodies. Defocused diffractions and reflections associated with salt bodies can help us estimate more accurate velocities at the top of the salt, particularly in the case of rough bodies. Moreover, defocused energy may be the most sensitive velocity information we have from under the salt, since most of the reflected energy recorded at the surface has only a narrow range of angles of incidence at the reflector, rendering the analysis of moveout ambiguous.

We begin with a summary of the wave-equation MVA methodology, specialized to diffraction focusing, followed by synthetic and real-data examples from seismic and GPR applications.

THEORY OF WAVE-EQUATION MVA

In this section, we summarize the main elements of wave-equation MVA by closely following the theory presented in Sava and Biondi (2004a,b). The reader familiar with those details can skip to the next section. We begin with a quick discussion of wavefield scattering in the context of wavefield extrapolation. Then we define the objective function of our method and the linearized image perturbations that enable us to overcome the limitations of the first-order Born approximation.

Wavefield scattering

Imaging by wavefield extrapolation is based on recursive continuation of the wavefields $\mathcal{U}$ from a given depth level to the next by means of an extrapolation operator $\mathbf{E}$:

$$\mathcal{U}_{z+\Delta z} = \mathbf{E}_z[\mathcal{U}_z]. \tag{1}$$

We use the following notation conventions: $\mathbf{A}[x]$ stands for the linear operator $\mathbf{A}$ applied to x, and $f(x)$ stands for function f of argument x.

At any depth z, the wavefield $\tilde{\mathcal{U}}$ extrapolated through the background medium characterized by the background slowness $\tilde{s}$ interacts with medium perturbations Δs creating wavefield perturbations $\Delta\mathcal{V}$:

$$\Delta\mathcal{V}_z = \mathbf{S}_z(\tilde{\mathcal{U}}_z)(\Delta s_z). \tag{2}$$

In equation 2, $\mathbf{S}$ is a scattering operator relating slowness perturbations to wavefield perturbations. The total wavefield perturbation at depth $z + \Delta z$ is the sum of the perturbation accumulated down to depth z from all depths above ($\Delta\mathcal{U}_z$), plus the scattered wavefield from depth $\Delta\mathcal{V}_z$ extrapolated one depth step Δz:

$$\Delta\mathcal{U}_{z+\Delta z} = \mathbf{E}_z[\Delta\mathcal{U}_z] + \mathbf{E}_z[\mathbf{S}_z(\tilde{\mathcal{U}}_z)(\Delta s_z)]. \tag{3}$$

Recursive equation 3 is used to compute a wavefield perturbation $\tilde{\mathcal{U}}_z$ given a precomputed background wavefield and a slowness perturbation Δs_z. In a more compact notation, we can write equation 3 as follows:

$$\Delta\mathcal{U} = (\mathbf{1} - \mathbf{E})^{-1}\mathbf{E}\mathbf{S}\Delta s, \tag{4}$$

where $\Delta\mathcal{U}$ and Δs stand, respectively, for the global wavefield and slowness perturbations and where $\mathbf{E}$, $\mathbf{S}$, and $\mathbf{1}$ are, respectively, the wavefield extrapolation and the scattering and identity operators. In our current implementation, $\mathbf{S}$ refers to a first-order Born scattering operator.

Wavefield perturbation $\Delta\mathcal{U}$ is used to compute an image perturbation $\Delta\mathcal{R}$ by applying an imaging condition, $\Delta\mathcal{R} = \mathbf{I}\Delta\mathcal{U}$. For example, the imaging operator $\mathbf{I}$ can be a simple summation over frequencies. If we accumulate all scattering, extrapolation, and imaging into a single operator $\mathbf{L} = \mathbf{I}(\mathbf{1} - \mathbf{E})^{-1}\mathbf{E}\mathbf{S}$, we can write a simple linear expression relating $\Delta\mathcal{R}$ to Δs:

$$\Delta\mathcal{R} = \mathbf{L}\Delta s. \tag{5}$$

Wave-equation MVA uses equation 5 to estimate a perturbation of the slowness model from a perturbation of the migrated image by minimizing the objective function

$$J(\Delta s) = \|\mathbf{W}(\Delta\mathcal{R} - \mathbf{L}\Delta s)\|^2, \tag{6}$$

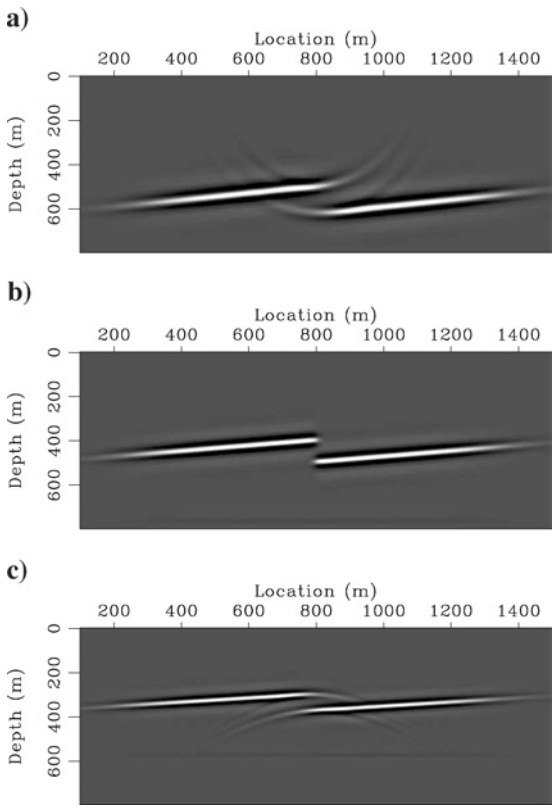

Figure 3. Migration of data generated from an earth model with sharp truncations. Images obtained by wave-equation migration with (a) fast velocity, (b) correct velocity, and (c) slow velocity.

where **W** is a weighting operator related to the inverse of the data covariance, indicating the reliability of the data residuals. Since, in most practical cases, the inversion problem is not well conditioned, we need to add constraints on the slowness model via a regularization operator **A**. In these situations, we use the modified objective function

$$J(\Delta s) = \|\mathbf{W}(\Delta\mathcal{R} - \mathbf{L}\Delta s)\|^2 + \epsilon^2\|\mathbf{A}\Delta s\|^2. \qquad (7)$$

The regularization operator **A** penalizes rough features of the model, and ϵ is a scalar parameter that balances the relative importance of the data $\mathbf{W}(\Delta\mathcal{R} - \mathbf{L}\Delta s)$ and model $\mathbf{A}\Delta s$ residuals.

An essential element of our velocity analysis method is the image perturbation $\Delta\mathcal{R}$. For purposes of the optimization problem in equation 7, this object is known and precomputed, together with the background wavefield used by the operator **L**.

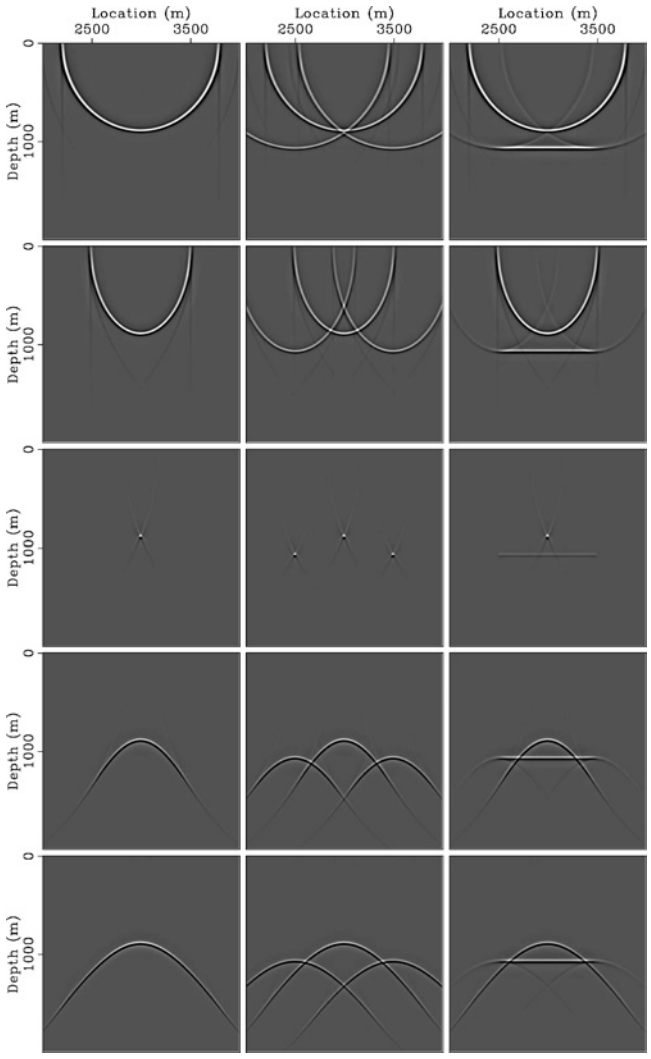

Figure 4. Residual migration applied to simple synthetic models. From top to bottom, the images correspond to the ratios $\rho = 0.7$, 0.8, 0.9, 1.0, and 1.1. The middle row corresponds to the correct velocity when all diffractors are focused.

Image perturbations

A simple way to define $\Delta\mathcal{R}$ is to take the image obtained with the background slowness and improve it by applying an image enhancement operator. Many techniques can be used to obtain an enhanced image: we choose residual migration to simultaneously flatten angle gathers and focus diffractions observed in common-offset sections.

Although, in principle, focusing in space (along the midpoint axis) and focusing in offset are both velocity indicators and should be used together to achieve the highest accuracy, in this article we emphasize MVA that only focuses diffractions along the spatial axes.

We use prestack Stolt residual migration (Stolt, 1996; Sava, 2003) as the image enhancement operator **K**. This residual migration operator applied to the background image creates new images $\mathcal{R}$, functions of a scalar parameter ρ that represents the ratio of a new slowness model relative to the background one:

$$\mathcal{R} = \mathbf{K}(\rho)[\mathcal{R}_b]. \qquad (8)$$

We can now take the image perturbation to be the difference between the improved image $\mathcal{R}$ and the background image $\mathcal{R}_b$:

$$\Delta\mathcal{R} = \mathcal{R} - \mathcal{R}_b. \qquad (9)$$

The main challenge with this method of constructing image perturbations for wave-equation MVA is that $\mathcal{R}$ and $\mathcal{R}_b$ can be too different from one another. In these situations, corresponding reflectors can get out of phase, a phenomenon usually referred to as cycle skipping. Thus, we risk violating the requirements of the first-order Born approximation that is central for our MVA technique (Sava and Biondi, 2004a). For example, we might end up subtracting unfocused from focused diffractions at different locations in the image.

We address this challenge by using linearized image perturbations. We run residual migration for a large number of parameters ρ and pick at every location the value where the image is best focused. Then we estimate at every point the gradient of the image relative to the ρ parameter and construct the image perturbations using the following relation:

$$\Delta\mathcal{R} \approx \mathbf{K}'|_{\rho=1}[\mathcal{R}_b]\Delta\rho, \qquad (10)$$

where, by definition, $\Delta\rho = 1 - \rho$.

The main benefit of constructing image perturbations with equation 10 is that we avoid the danger of subtracting out-of-phase images. In fact, we do not subtract images at all; we simply construct the image perturbation corresponding to a particular map of residual migration parameters ρ. In this way, we honor the information from residual migration while being safe relative to the limits of the first-order Born approximation.

Figure 4 and 5 illustrate the MVA methodology using residual migration and linearized image perturbations. Figure 4 shows three simple models with diffractors and reflectors with a constant velocity $v = 2000$ m/s. We use these three models to illustrate different situations: an isolated diffractor at location $x = 3000$ m and depth $z = 900$ m (Figure 4, left), the same diffractor flanked by other diffractors at $z = 1100$ m (Figure 4, middle), and finally, the same diffractor next to a short reflector at $z = 1100$ m, (Figure 4, right).

We migrate each synthetic data set with an incorrect velocity, $v = 1800$ m/s, and then apply residual migration with various velocity ratios, from $\rho = 0.7$ to $\rho = 1.1$. From top to bottom, each row corresponds to a different velocity ratio as follows: 0.7, 0.8, 0.9, 1.0, and 1.1. For all residual migration examples, we have eliminated the vertical shift induced by the different velocities, such that only the diffraction component of residual migration is left. Thus, we can better compare focusing of various events without being distracted by their vertical movement.

The best focused images correspond to $\rho = 0.9$. Since both the backgrounds and the perturbations are constant, the images focus at a single ratio parameter. The ratio difference between the original images at $\rho = 1.0$ and the best focused images at $\rho = 0.9$ is $\Delta\rho = 0.1$. In general, the images focus at different ratios at different locations, causing $\Delta\rho$ to be a spatially variable function.

Using the background images and the measured $\Delta\rho$, we compute the linearized image perturbations (Figure 5, top). Using the wave-equation MVA operator, we compute the corresponding slowness perturbations after 15 linear iterations (Figure 5, bottom). The image perturbations closely resemble the background image (Figure 4, fourth row from top), with a $\pi/2$ phase shift and appropriate scaling with the measured $\Delta\rho$.

For all models in Figures 4 and 5, we measure focusing on a single event (the main diffractor at $x = 2000$ m and depth $z = 900$ m) but assign the computed $\Delta\rho$ to other elements of the image in the vicinity of this diffractor. The rationale for doing so is that we can assume all elements at a particular location are influenced by roughly the same part of the model. Therefore, not only is a priori separation of the diffractors from the reflectors not required, but the additional elements present in the image perturbation add robustness to the inversion.

EXAMPLES

The first example concerns a synthetic data set obtained by acoustic finite-difference modeling over a salt body. Although in this example we use our technique to constrain the top of the salt, we emphasize that the same technique can be used in any situation where diffractions or defocused events are present. For example, in subsalt regions where angular coverage is small, uncollapsed diffractions carry substantial information that is disregarded in typical MVA methodologies.

The second example is a single-channel, constant-offset GPR field data set. Most GPR data sets are single channel, and no method has thus far been developed to estimate a reasonable interval velocity model in the presence of lateral velocity variations. Typically, the velocity estimated by Dix inversion at sparse locations along the survey line is smoothly extrapolated, although this is not optimal from an imaging point of view.

Delineation of rough salt bodies

Figure 6 shows the 2D zero-offset data used for velocity analysis to delineate the top of the rough salt body. The section contains a large number of diffractors and defocused specular energy, whose focusing allows us to constrain the overburden velocity model.

Figures 7a and 7b depict the starting velocity model and the initial image obtained by zero-offset migration. The starting velocity is a typical Gulf of Mexico $v(z)$ function from the ocean floor. Defocused energy is visible at the top of the salt, indicating that the velocity in the overburden is not accurate. Such defocusing causes inaccuracies in our top-of-salt picks and therefore degrades imaging at depth.

As in the preceding synthetic example, we apply residual migration on the background image (Figure 7a). Figure 8 shows the images after residual migration with various velocity ratios (Sava, 2003). From top to bottom, the ratios are 1.04, 1.00, 0.96, 0.92, and 0.88. At $\rho = 1.00$ we recover the initial image. Different parts of the image come into focus at different values of the velocity ratio.

Figure 9a shows the picked velocity ratios at various locations in the image. The dark background corresponds to picked $\Delta\rho = 0$, and the gray shades correspond to $\Delta\rho$ between 0 and 0.08. Figure 9b shows a map of the weights $\mathbf{W}$ associated with each picked value. The white background corresponds to $\mathbf{W} = 0$, indicating low confidence in the picked values, and the black regions correspond to $\mathbf{W} = 1$, indicating

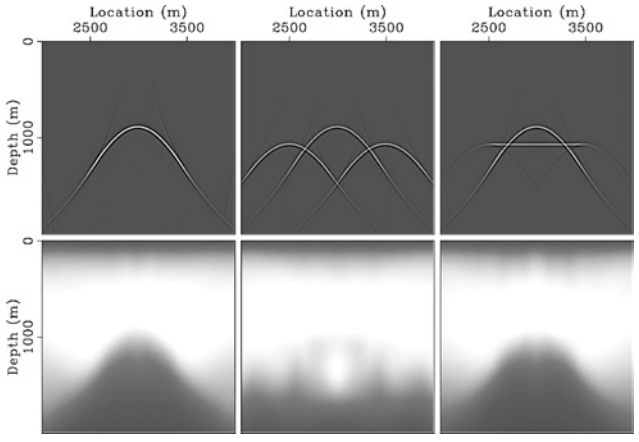

Figure 5. MVA for the simple synthetic models in Figure 4. The top row depicts image perturbations, and the bottom row depicts slowness perturbations obtained after 15 linear iterations.

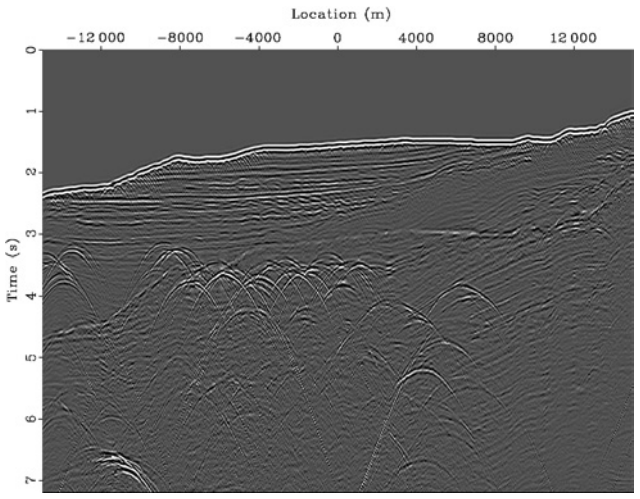

Figure 6. Zero-offset synthetic data used for focusing MVA.

high confidence in the picked values. In this example, we disregard regions where diffractions were not picked. All other regions receive an arbitrary ratio value but also a low weight, such that they do not influence the inversion. Exceptions include the ocean floor, for which we assign a high weight of the picked ratio $\rho = 1.0$, and a few other reflectors for which we do not have any focusing information.

Figure 9d shows the slowness perturbation obtained after 20 iterations of zero-offset inversion from the image perturbation in Figure 9c. The image perturbation is nonzero only in the regions where we picked diffractions, as indicated by Figure 9. The smooth slowness perturbation is further constrained by our regularization operator, which is a simple Laplacian penalizing the rough portions of the model. Figures 7c and 7d show the updated slowness model and the zero-offset migrated image corresponding to the updated model. Most of the energy at the top of the salt has been focused, and the rough top of the salt can be easily picked.

Figure 10 shows prestack migrated images using the initial velocity model (Figure 10a) and the one updated using zero-offset focusing (Figure 10b). The top panels depict stacked seismic images, and the bottom panels depict angle-domain common-image gathers (Sava and Fomel, 2003). The reflectors in the angle gathers show substantial bending after migration with the initial velocity, but they are mostly flat after migration with the updated velocity. Figure 11 shows two angle gathers at $x = -2350$ m from the images obtained with the initial velocity model and the updated velocity model. The angle gather in Figure 11a corresponds to a notch in the top of the salt and is difficult to use for velocity analysis. However, after migration with the updated velocity model (Figure 11b), the reflectivity in the angle gather is much simpler and the small residual moveouts can be picked for velocity updates.

A comparison of Figures 7d and 10b shows a potential limitation of our technique in the presence of prismatic waves (Biondi, 2003). Both images are obtained with the same velocity, the first one with zero-offset data and the second one with

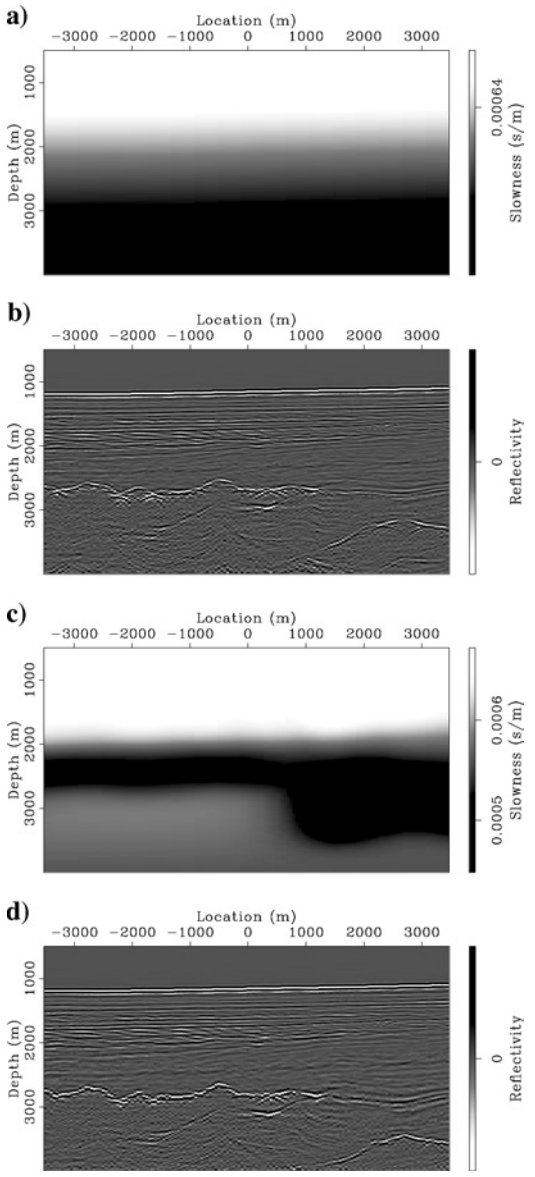

Figure 7. Zero-offset migrated image for the synthetic data in Figure 6: (a) initial velocity model and (b) corresponding migrated image; (c) updated velocity model and (d) corresponding migrated image.

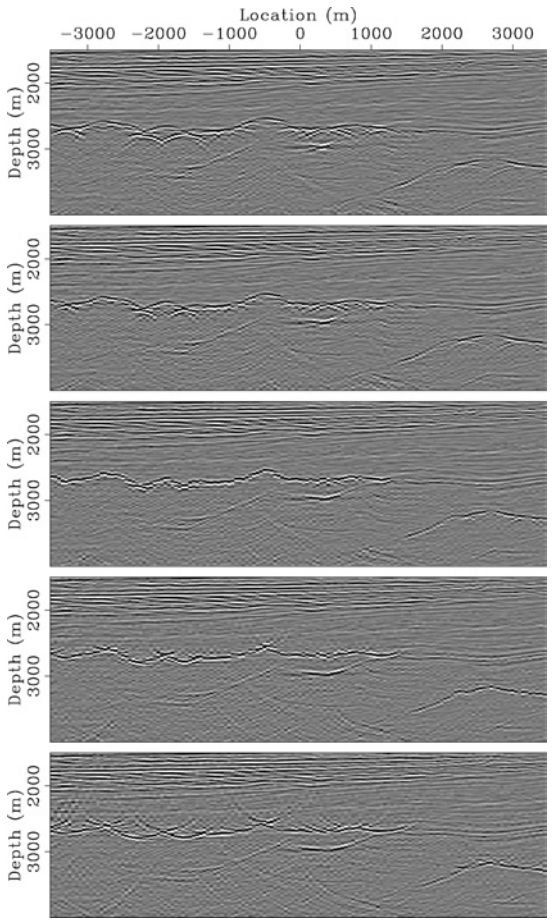

Figure 8. Residual migration applied to the image migrated with the initial velocity model, Figure 7. From top to bottom, the images correspond to the ratios $\rho = 1.04$, 1.00, 0.96, 0.92, and 0.88.

prestack data. The imaging artifacts visible at the base of the deep salt canyons in Figure 7 are created by prismatic waves that are not properly imaged from zero-offset data. Prismatic waves (Figure 12) are better (though not perfectly) handled by full prestack migration; thus, the artifacts are not visible in the prestack-migrated image shown in Figure 10b. Since these artifacts resemble unfocused diffractions, they may mislead the analysis of the residual migrated images and be interpreted as velocity inaccuracies.

Imaging GPR data

Our next example concerns a zero-offset GPR data set over a lava flow region. In this situation, diffraction focusing is the only option available for MVA. The data depicted in Figure 13 show many diffractions spread over the entire data set. A few obvious ones are at $x = 8.5$ m, $t = 22$ ns, and at $x = 10.5$ m, $t = 23$ ns.

The same MVA procedure as the one described for the preceding example is used. Figure 14b shows the initial image obtained by migration with a constant velocity ($v = 0.2$ m/ns depicted in Figure 14a), and Figure 14d shows the final image obtained by migration with the updated velocity model depicted in Figure 14c. We notice that the updated image is vertically compressed, since the velocity update leads to faster migration velocities. Most of the diffractions have been collapsed, indicating that focusing analysis improved the accuracy of the velocity model.

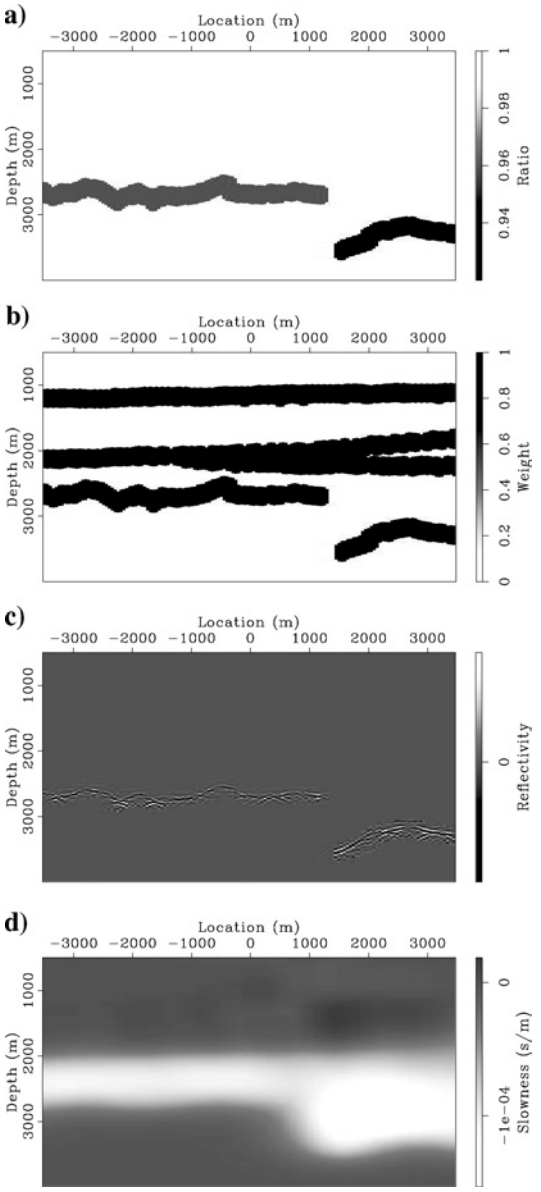

Figure 9. (a) Residual migration picks and (b) the associated confidence weights. Slowness perturbation (d) is derived from an image perturbation (c) obtained from the background image in Figure 7b and the velocity ratio picks in (a).

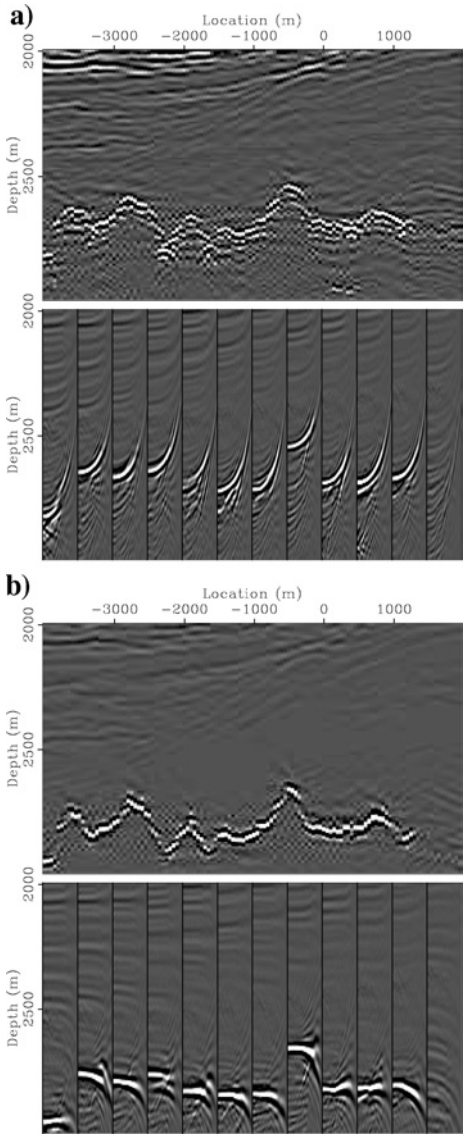

Figure 10. Prestack migrated images using (a) the initial velocity model and (b) the updated velocity model. The top panels depict image stacks, and the bottom panels depict angle-domain common-image gathers.

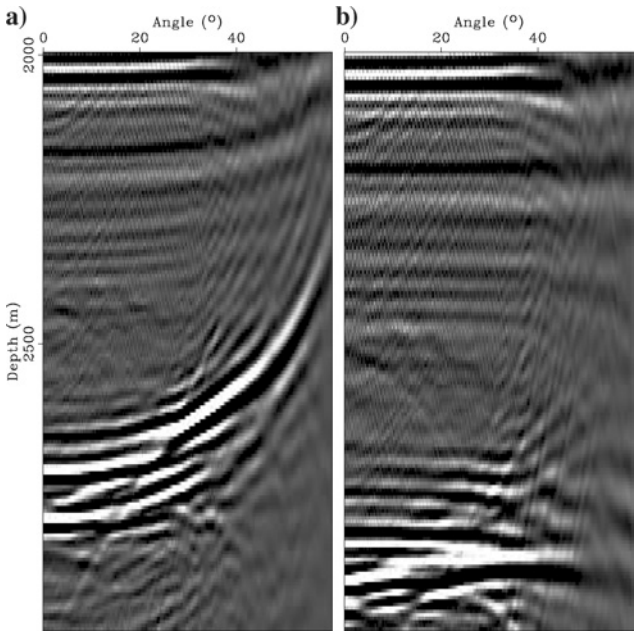

Figure 11. Angle-domain common-image gather obtained after migration with (a) the initial velocity model and (b) the updated velocity model.

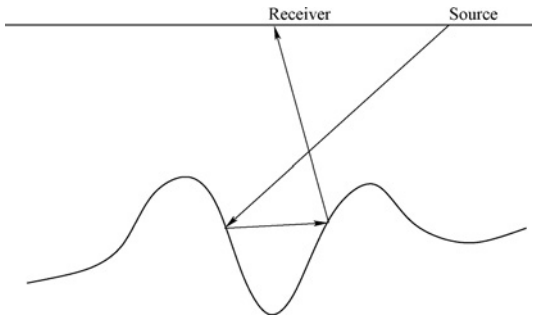

Figure 12. Prismatic waves at a rugose top salt.

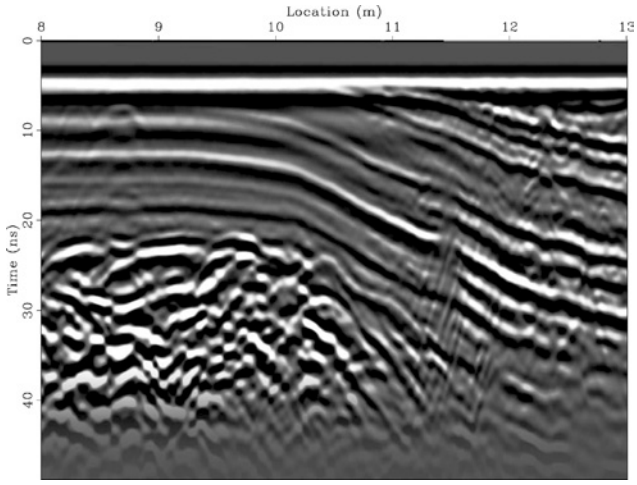

Figure 13. Zero-offset GPR data used for focusing MVA.

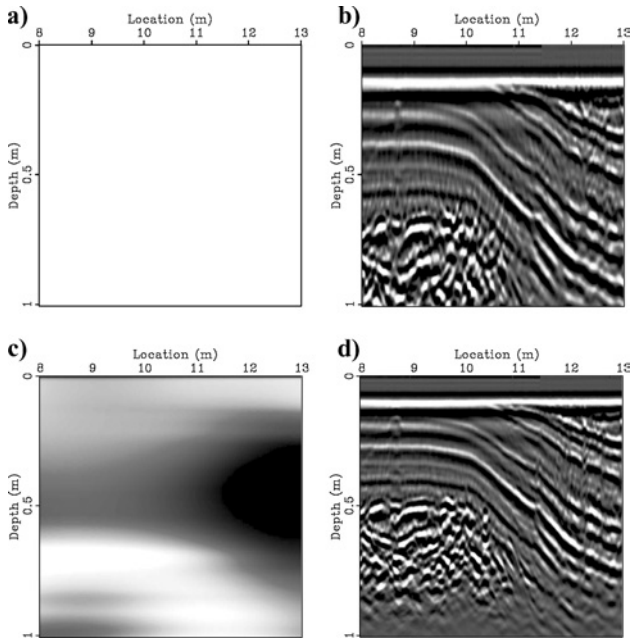

Figure 14. Zero-offset migrated images for the data in Figure 13 using the initial constant velocity (a)-(b) and the updated velocity (c)-(d).

CONCLUSIONS

Defocused diffracted and reflected events contain useful velocity information usually overlooked by conventional MVA methods, which use flatness of common-image gathers as the only criterion for the accuracy of migration velocity. In this article, we demonstrate that accurate interval-velocity updates can be estimated by inverting the results of a residual-focusing analysis of migrated diffracted events. To convert residual-focusing measurements into interval-velocity updates, we use the wave-equation MVA methodology, which is ideally suited for this task because it inverts image perturbations directly without requiring a precise estimate of the reflector geometry. In contrast, ray-based MVA methods require that the reflector geometry be provided by interpreting the migrated image. However, since the interpretation of partially focused diffracted events is extremely difficult, ray-based methods are never used for diffraction-focusing velocity analysis.

Our seismic data example demonstrates how the proposed method exploits the velocity information contained in the reflected wavefield generated by a rugose salt–sediment interface. These kinds of events are present in many salt-related data sets, and using this diffracted energy to further constrain the velocity model might significantly improve the final imaging results.

The GPR data example demonstrates the potential of our method for improving the imaging of such data. We demonstrate that the model obtained by extracting interval velocity information from the diffracted events improves the reflector continuity in the migrated image and facilitates geologic interpretation of the images. Since a large number of GPR data sets are limited to constant-offset recordings, the possibility of using diffractions to define the lateral velocity variations substantially widens the effectiveness of GPR surveys in complex geologic environments.

ACKNOWLEDGMENTS

We acknowledge the financial support of the sponsors of the Stanford Exploration Project (SEP). We also acknowledge Frederic Billette (BP) for providing the synthetic salt-dome data set and Antoine Guitton (SEP) for suppressing multiples in this data set. Kevin Williams of the Smithsonian Institution in Washington, D.C., provided the GPR data set.

REFERENCES

Al-Yahya, K. M., 1989, Velocity analysis by iterative profile migration: Geophysics, **54**, 718–729.

Billette, F., S. L. Begat, P. Podvin, and G. Lambare, 2003, Practical aspects and applications of 2D stereotomography: Geophysics, **68**, 1008–1021.

Biondi, B. L., 2003, 3-D seismic imaging: <http://sepwww.stanford.edu/sep/biondo/Lectures/index.html>.

Biondi, B., and P. Sava, 1999, Wave-equation migration velocity analysis: 69th Annual International Meeting, SEG, Expanded Abstracts, 1723–1726.

Dahlen, F. A., S. H. Hung, and G. Nolet, 2000, Frechet kernels for finite frequency traveltimes — I. Theory: Geophysical Journal International, **141**, 157–174.

de Vries, D., and A. J. Berkhout, 1984, Velocity analysis based on minimum entropy: Geophysics, **49**, 2132–2142.

Etgen, J., 1993, Interval velocity estimation using residual prestack migration: 63rd Annual International Meeting, SEG, Expanded Abstracts, 669–672.

Harlan, W. S., J. F. Claerbout, and F. Rocca, 1984, Signal/noise separation and velocity estimation: Geophysics, **49**, 1869–1880.

Khaidukov, V., E. Landa, and T. Moser, 2004, Diffraction imaging by focusing-defocusing: An outlook on seismic superresolution: Geophysics, **69**, 1478–1490.

Landa, E., and S. Keydar, 1998, Seismic monitoring of diffraction images for detection of local heterogeneities: Geophysics, **63**, 1093–1100.

Papziner, U., and K. P. Nick, 1998, Automatic detection of hyperbolas in georadargrams by slantstack processing and migration: First Break, **16**, 219–223.

Pipan, M., E. Forte, G. D. Moro, M. Sugan, and I. Finetti, 2003, Multifold ground-penetrating radar and resistivity to study the stratigraphy of shallow unconsolidated sediments.: The Leading Edge, **22**, 876–881.

Pratt, R. G., 1999, Seismic waveform inversion in the frequency domain — Part 1: Theory and verification in a physical scale model: Geophysics, **64**, 888–901.

Sava, P., 2003, Prestack residual migration in the frequency domain: Geophysics, **67**, 634–640.

Sava, P., and B. Biondi, 2004a, Wave-equation migration velocity analysis — I: Theory: Geophysical Prospecting, **52**, 593–606.

———, 2004b, Wave-equation migration velocity analysis — II: Subsalt imaging examples: Geophysical Prospecting, **52**, 607–623.

Sava, P., and S. Fomel, 2002, Wave-equation migration velocity analysis beyond the Born approximation: 72nd Annual International Meeting, SEG, Expanded Abstracts, 2285–2288.

———, 2003, Angle-domain common image gathers by wavefield continuation methods: Geophysics, **68**, 1065–1074.

Soellner, W., and W. Yang, 2002, Diffraction response simulation: A 3D velocity inversion tool: 72nd Annual International Meeting, SEG, Expanded Abstracts, 2293–2296.

Stolt, R. H., 1996, Short note — A prestack residual time migration operator: Geophysics, **61**, 605–607.

Stork, C., 1992, Reflection tomography in the postmigrated domain: Geophysics, **57**, 680–692.

Tarantola, A., 1986, A strategy for nonlinear elastic inversion of seismic reflection data: Geophysics, **51**, 1893–1903.

Vasco, D. W., J. E. Peterson, and K. H. Lee, 1997, Ground-penetrating radar velocity tomography in heterogeneous and anisotropic media: Geophysics, **62**, 1758–1773.

Woodward, M. J., 1992, Wave-equation tomography: Geophysics, **57**, 15–26.